minerals

MDPI

Article

Twinning Impact on the Structure and Hypotheses on the Growth Mechanism of Kermesite: Insights from Yunnan, China

Hong Yu [1,2,*], Denghong Wang [1], Zeying Zhu [1], Wenyuan Li [3], Dong Wang [1], Zhenyu Chen [1], Yike Li [1] and Changhui Ke [1]

[1] MNR Key Laboratory of Metallogeny and Mineral Assessment, Institute of Mineral Resources, Chinese Academy of Geological Sciences, Beijing 100037, China; wangdenghong@vip.sina.com (D.W.); zhuzeying_nju@163.com (Z.Z.); wdong14@126.com (D.W.); czy7803@163.com (Z.C.); like430@cags.ac.cn (Y.L.); kechanghuicags@126.com (C.K.)
[2] China University of Geosciences (Beijing), Xueyuan Road 29, Beijing 100083, China
[3] Key Laboratory for the Study of Focused Magmatism and Giant Ore Deposits, Ministry of Land and Resources, Xi'an Center of China Geological Survey, Xi'an 710054, China; xalwenyuan@126.com
* Correspondence: coime_yh@hotmail.com

Abstract: Kermesite (Sb_2S_2O), a needle-like unstable secondary oxysulfide, has made visible advancements in optimizing its triclinic crystal system through twinning discovery. However, research on twinning behavior at micro and nano scales, including its growth mechanisms and impact on kermesite morphologies, remains notably scarce. Our study focuses on kermesite crystal clusters from a private collection in Yunnan, China, confirming the chemical formula as $Sb_2S_{1.97}O_{1.03}$ through EPMA. Single-crystal XRD yielded refined unit cell parameters (a = 8.153(5) Å, b = 10.717(7) Å, c = 5.796(3) Å; α = 102.836(10)°, β = 110.556(8)°, γ = 100.999(12)°), revealing space group $P\bar{1}$ with Z = 4 and indicating twinning with a ratio of 27.4%. Remarkably, a Transmission Electron Microscope (TEM) provided the first direct observation of twinning in natural kermesite, revealing rotational twins with varying widths and lengths (ranging from 100 nm to several millimeters). Analysis and simulation elucidated that rotational twins, generated by a 180° rotation, align with the mineral's elongation direction along the $[Sb_2S_2O_4]_n$ chains (a-axis), challenging the conventional long-axis direction (b-axis) for crystal growth. This study proposes a symbiotic relationship between kermesite growth and twinning, suggesting that the observed X-shaped growth in crystal clusters results from the collaboration of single crystals (growing along b) and twins (growing along a) in the unit cell. These findings contribute to our understanding of kermesite's structural complexities and the potential growth and formation mechanism of crystal clusters.

Keywords: kermesite; twinning; TEM; mineral growth mechanisms

Citation: Yu, H.; Wang, D.; Zhu, Z.; Li, W.; Wang, D.; Chen, Z.; Li, Y.; Ke, C. Twinning Impact on the Structure and Hypotheses on the Growth Mechanism of Kermesite: Insights from Yunnan, China. *Minerals* **2024**, *14*, 505. https://doi.org/10.3390/min14050505

Academic Editor: Thomas N. Kerestedjian

Received: 12 April 2024
Revised: 4 May 2024
Accepted: 4 May 2024
Published: 10 May 2024

1. Introduction

Kermesite, Sb_2S_2O, an unstable secondary oxysulfide, is generally considered to be an alteration product of stibnite, often associated with other secondary antimony minerals, such as stibnite (Sb_2S_3), antimony (Sb), sénarmontite (isometric Sb_2O_3), valentinite (Sb_2O_3), cervantite ($Sb^{3+}Sb^{5+}O_4$), stibiconite [$Sb^{3+}Sb_2^{5+}O_6(OH)$], etc. [1–5]. Kermesite forms acicular crystals with a metallic or semi-metallic luster, often appearing dark red, purplish red, bright grey, or dark. These crystals are typically believed to grow along the long axis, often reaching lengths of several millimeters and displaying perfect cleavage on {001}, which invariably leads to the formation of radiating and clustered shapes [1,6]. Their visually stunning appearance frequently attracts collectors to gather them as mineral crystals [1,4,7,8]. However, recent findings from our research have sparked inquiries into their growth direction, indicating the necessity for further investigation.

Since its official naming in 1832, the crystal structure of kermesite has undergone multiple revisions by various authors. These revisions include the transition from Wolfe's (1939)

initial refined monoclinic structure to Tavora's (1949) monoclinic and triclinic structures, and finally, to Kupčìκ's (1967) complex triclinic single-cell structure [6,9,10]. The presence of twins in kermesite, resulting in pseudo-monoclinic symmetry, posed a challenge in resolving the optimal primary singlet structure. The breakthrough came in 1987 when Bonazzi et al. discovered the twin structure in kermesite. They refined the primary singlet's triclinic structure using single-crystal XRD data, determining a space group of $P\bar{1}$ with Z = 4 and cell parameters including the following: a = 8.1416(3) Å, b = 10.6968(3) Å, c = 5.7835(2) Å, α = 102.758(3)°, β = 110.657(3)°, γ = 101.020(3)° [6,9–11]. Hybler further refined the structure data of kermesite from Slovakia [6], using the structural models proposed by Kupčìκ (1967) [10] and Bonazzi P et al. (1987) [9], noting that the varying presence of twins in the studied samples suggested the construction of a face-centered pseudo-monoclinic structure. This structure is characterized by a non-standard eight-fold primary base monolayer structure, creating a de-symmetric ordered–disordered layered structure parallel to the bc plane and stacked along the a-axis direction [6,11].

Kermesite is a relatively common mineral in nature [1]. According to the Mindat database [12], there are 239 specific locations worldwide where this mineral is found. Among these, the locations of kermesite in four provinces and six regions of China are listed. However, existing reports mainly categorize kermesite in China either as a coexisting mineral within ore deposits or as part of a mineral crystal collection. Notably, there have been no reports on the mineral crystal structure of kermesite produced in China. The samples in this study are sourced from the personal collection of Professor Wang Denghong, originating from antimony deposits in Yunnan, China. The crystal structure information is refined through single-crystal XRD. Significantly, for the first time, twinning structures in kermesite are directly observed and analyzed using TEM. This study aims to explore the potential growth and formation mechanism of kermesite crystal clusters at the nanoscale.

2. Materials and Methods

2.1. Sample Source

The kermesite analyzed in this study was sourced from the private collection of Professor Wang Denghong, originating from Yunnan, China. The hand specimen measures approximately 5 × 7 × 7 cm and displays a distinctive cluster-like structure. Its visual appeal is striking, showcasing a bright gray color overall. On the hand specimen, individual kermesite crystals appear columnar or needle-like, with crystals interlacing and growing in a crosshatch pattern, as depicted in Figure 1a. These crystals can extend to several centimeters in length while maintaining a thickness and width generally less than 5 mm. Notably, some of the larger columnar structures boast a thickness and width ranging around 2 mm. Using tweezers, several intersecting single crystals were carefully extracted from the cluster for experimental analysis, as depicted in Figure 1b,c.

2.2. Analytical Methods

Electron probe micro-analyzer (EPMA). EPMA analysis was conducted at the Electron Probe Laboratory of the Institute of Mineral Resources, Chinese Academy of Geological Sciences. The instrument employed for this analysis was the JXA-8230 (model, manufacturer, city, state abbreviation if USA or Canada, country JEOL, Tokyo, Japan), equipped with a wave dispersive spectrometer and an X-max energy dispersive spectrometer. Because of the relatively poor electrical conductivity of kermesite, the sample surfaces underwent carbon coating before testing. Point analysis was performed on the samples under the following conditions: operating voltage of 20 kV, probe current of 20 nA, and an electron beam spot size of 5 μm. Standard samples used for testing included natural minerals and alloy samples, specifically chalcopyrite (Fe, Cu in $CuFeS_2$), pyrite (S in FeS_2), stibnite (Sb in Sb_2S_3), and arsenopyrite (As in FeAsS).

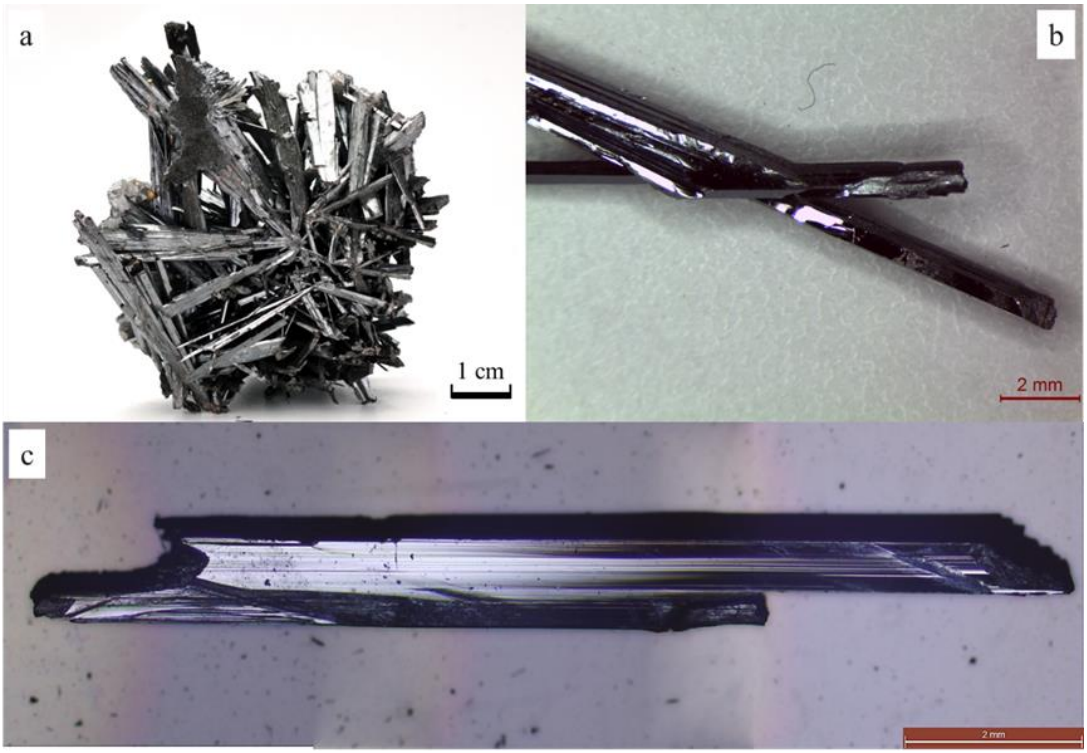

Figure 1. Morphology of kermesite crystals and single crystals. (**a**) Mineral collection of Professor Wang Denghong; (**b**) X-shaped crystals; (**c**) crystals of parallel growth.

Single-crystal X-ray diffraction (XRD). Needle-shaped kermesite crystals measuring 0.16 × 0.08 × 0.05 mm were selected for X-ray crystallography. The analysis was conducted using a D8 Venture instrument (model, manufacturer, city, state abbreviation if USA or Canada, country Bruker AXS, Karlsruhe, Germany) equipped with a Bruker APEX-II CCD area detector for geometric intensity data collection. Throughout the data collection process, the temperature was maintained at 296.15 K. A 0.5 mm MonoCap collimator was used for direct Mo-Kα radiation (λ = 0.71073 Å) for data collection. The final unit cell parameters were refined from the collected 1580 strong reflections. The structure was resolved using the inherent phase method with the ShelXT structure solution program [13], which was implemented through Olex2 software v1.5 [14]. Structure refinement utilized the ShelXL optimization package [15,16], employing a least-squares method. The single-crystal structure data, experimental conditions, and other crucial information are presented in Table 1 (Column C). Our obtained structure aligns with the ID R060742 in the RRUFF database. Additionally, for comparative purposes, XRD single-crystal structure data for kermesite from the Pernek and Pezinok regions in western Slovakia, as reported by Hybler et al. (2013) [6], are listed in Table 1 (Columns A and B). Consistent with previous reports by Bonazzi et al. (1987) [9] and Hybler et al. (2013) [9], twinning in kermesite was observed in this X-ray crystallographic study, with an estimated twinning ratio of 27.4%.

Table 1. Refined single-crystal XRD structural data for kermesite (Mo Ka radiation, λ = 0.71073 Å) [6].

	A	**B**	**C**
	Data form Hybler and Durovic, 2013 [6]		Present study
Localities	Perneck and Pezinok, Slovakia		Yunnan, China
Empirical formula		Sb_2S_2O	
Space group		$P\bar{1}$	
a(Å)	8.1416	8.1372	8.153
b(Å)	10.6968	10.7840	10.717
c(Å)	5.7835	5.7840	5.796

Table 1. *Cont.*

	A	B	C
α	102.758°	102.787°	102.836°
β	110.657°	110.606°	110.556°
γ	101.02°	100.983°	100.999°
Cell volume (Å^3)	439.23	439.24	441.84
Z	4	4	4
Density (g/cm^3)	4.89	4.89	4.87
Crystal size (mm)	0.03 × 0.03 × 0.63	0.01 × 0.07 × 0.95	0.16 × 0.08 × 0.05
Absorption coefficient (mm^{-1})	13.056	13.056	12.979
Index ranges	$-11 \leq h \leq 12$, $-16 \leq k \leq 16$, $-8 \leq l \leq 8$	$-11 \leq h \leq 12$, $-16 \leq k \leq 16$, $-8 \leq l \leq 8$	$-8 \leq h \leq 9$, $-13 \leq k \leq 6$, $-7 \leq l \leq 6$
Independent reflections	4465	4591	1580
T_{min}, T_{max}	0.1091, 0.6671	0.0480, 0.7789	0.548, 0.746
Goodness-of-fit on F^2	1.11	2.40	1.152
Final R indices [I > 2σ(I)]	R1 = 0.0216 wR2 = 0.0246	R1 = 0.0301 wR2 = 0.0365	R1 = 0.1000 wR2 = 0.2428
Final R indices (all data)	R1 = 0.0216 wR2 = 0.0247	R1 = 0.0301 wR2 = 0.0366	R1 = 0.1169 wR2 = 0.2531
Ratio of twin components	0.9454:0.0546(4)	0.5836:0.41464(8)	0.726:0.274(6)

Transmission Electron Microscope (TEM). TEM analysis was conducted at the Electron Microscopy Laboratory of the Institute of Mineral Resources, Chinese Academy of Geological Sciences. The instrument used for this analysis was the JEOL JEM-2100(HR) (model, manufacturer, city, state abbreviation if USA or Canada, country JEOL, Tokyo, Japan) equipped with a LaB6 filament, with a point resolution of 0.23 nm. The setup included double-tilt holders, a Gatan 832 CCD camera, and an Oxford Instrument Inca Energy100 Energy-Dispersive X-ray Spectroscopy (EDS) system. Because of the sensitivity of kermesite to electron beams, the operating voltage was set at both 200 kV and a low voltage of 80 kV. For EDS point composition analysis, a convergent electron beam spot of 25 nm was utilized. CrystalMaker X software version 10.8.3b2 was employed to analyze crystal structure data and CIF files, facilitating the visualization of kermesite's crystal structure [17]. Additionally, SingleCrystal 4 software version 4.1.9 was used to simulate corresponding Selected Area Electron Diffraction (SAED) patterns and Kikuchi diffraction patterns for further structural analysis.

The preparation process for kermesite TEM samples involved obtaining thin sections with a certain thickness through cleavage. These thin sections were then affixed and secured onto a Φ2.0 mm single-hole molybdenum (Mo) grid. Finally, a Gatan Model 695 ion milling instrument was utilized for dual-sided argon (Ar) ion polishing, preparing the samples into well-prepared TEM specimens.

3. Results

3.1. Chemical Composition

Based on the chemical formula Sb_2S_2O, the ideal chemical composition of kermesite (wt%) is calculated as follows: Sb (antimony) 75.24%, S (sulfur) 19.81%, and O (oxygen) 4.94%. The EPMA experimental composition data for kermesite are presented in Table 2. The measured contents of Sb and S closely match the theoretical values, indicating high purity of kermesite with very low trace element concentrations. To maintain charge balance in the theoretical chemical formula, assuming a 2 charge for the S ion in the ideal formula Sb_2S_2O, the structure parameters are normalized using the equation:

$$2Sb^{3+} = xS^{2-} + yO^{2-}$$

With this normalization, the calculated chemical formula for kermesite is determined as $Sb_2S_{1.97}O_{1.03}$. The detailed calculations are outlined in Table 2.

Table 2. EPMA elemental composition data of kermesite (wt%).

No.	Co	Sb	Bi	Ag	S	Fe	Ni	As	Cu	Zn	O	Total
1	0.006	75.430	0.035	0.015	19.546	0	0	0.221	0	0		95.253
2	0.008	75.317	0	0.006	19.643	0	0	0.236	0	0		95.240
3	0	75.306	0	0	19.644	0.002	0	0.167	0	0.004		95.123
4	0	75.023	0	0	19.604	0.023	0.001	0.222	0.004	0.027		94.904
5	0	75.150	0	0	19.415	0	0	0.305	0	0.169		95.039
6	0	74.838	0	0	19.397	0.004	0	0.182	0	0.039		94.480
Average		75.177			19.542			0.222			5.068 [1]	100.133
Standard Deviation		0.219		0.111		0.048			0.289			
Atom Weight		121.750			32.064			74.922			15.999	
Mole Fraction		0.617			0.609			0.003			0.317	
Structure Coefficient [2]		2.03			2.00						1.04	
		Measured Chemistry [3]							$Sb_2S_{1.97}O_{1.03}$			

Note: [1] O adjusted to achieve charge balance, then normalized to 2 Sb. [2] The structure coefficient is calculated with S as 2, the total molar fractions $F_{total} = 2/(\text{mole fraction})_s$, and the structural coefficient of Sb and O are $F^*[(\text{mole fraction})_i$, i = Sb or O]. [3] The measured chemistry formula is normalized by the cation number Sb^{3+} as 2.

3.2. Crystal Structure Refinement

The refined single-crystal XRD structural data for kermesite, as presented in Table 1 (Column C), reveals a triclinic structure with the space group $P\bar{1}$. The lattice parameters a, b, and c are determined to be 8.153(5) Å, 10.717(7) Å, and 5.796(3) Å, respectively. The angles α, β, and γ are measured as 102.836(10)°, 110.556(8)°, and 100.999(12)°. It is noteworthy that the structures of kermesite from China are entirely equivalent to the kermesite structure reported by Hybler et al. (2013) [6] and Bonazzi et al. (1987) [9] from Slovakia, as depicted in Table 1 (Columns A and B).

The refined crystal structure of kermesite provides insight into atomic occupancy within the lattice, detailing atomic distances and angles between the cation Sb and neighboring anions S and O, as illustrated in Tables 3 and 4. Notably, the distances between Sb and the adjacent O range from 2.00 to 2.20 Å, while the distances between Sb and the neighboring S fall within the range of 2.4 to 2.7 Å. The crystal structure projection along [100], [001], and [011] are depicted in Figure 2. In the structure, Sb occupies four positions, labeled Sb(1), Sb(2), Sb(3), and Sb(4), respectively. They coordinate with the neighboring S and O to form two types of polyhedra including lozenge and pyramidal [6]. In these polyhedra, the ionic radius of Sb ions is 0.76 Å, S is 1.84 Å, and O is 1.36 Å [18]. Each Sb(1) and Sb(2) coordinates closely with three O and one S neighbors, forming $[SbSO_3]$ lozenge polyhedron [19]. The juxtaposition of two oppositely oriented $[Sb_SO_3]$ polyhedrons along an edge results in the elongation of $[Sb_2S_2O_4]_n$ chains along the a-axis, as shown in Figure 2b. Furthermore, each S atom is associated with two neighboring Sb atoms. Sb(3) and Sb(4) engage with three S neighbors, forming $[Sb_4S_6]$ pyramidal ribbons. These $[Sb_4S_6]$ ribbons interconnect with $[Sb_2S_2O_4]_n$ chains via O, leading to the formation of $[Sb_4S_4O_2]_n$ layers that extend infinitely in the ab plane, as shown in Figure 2.

Table 3. Crystallographic coordinates, equivalent/isotropic (Å2), and anisotropic displacement parameters (Å2) of kermesite.

Atom	x	y	z	U(eq)	U11	U22	U33	U23	U13	U12
O1	0.0980(30)	0.4320(20)	0.4640(50)	0.009(1)	0.015	0.015	0.015	0.0046	0.006	0.0046
O2	0.4130(30)	0.5720(20)	0.5690(40)	0.009(1)	0.011	0.011	0.011	0.0033	0.005	0.0032
S1	0.1911(11)	0.2966(8)	0.9992(17)	0.019(1)	0.011	0.011	0.017	−0.001	0.009	0.001
S2	0.2939(13)	0.6945(8)	0.0158(17)	0.021(1)	0.011	0.016	0.016	0.002	0.005	0.006
S3	0.0450(13)	0.9097(8)	0.7248(17)	0.013(2)	0.0134	0.0132	0.0138	0.0039	0.0054	0.0041
S4	0.4782(13)	0.0892(8)	0.2715(16)	0.015(2)	0.017	0.007	0.012	−0.001	0.006	0.006

Table 3. *Cont.*

Atom	x	y	z	U(eq)	U11	U22	U33	U23	U13	U12
Sb1	0.3387(4)	0.3702(2)	0.4829(4)	0.014(2)	0.006	0.0077	0.0138	0.0008	0.0049	0.0041
Sb2	0.1671(4)	0.6312(2)	0.5358(4)	0.012(2)	0.0063	0.0077	0.013	0.0008	0.0046	0.0043
Sb3	0.1240(4)	0.8563(4)	0.1333(5)	0.015(5)	0.0085	0.027	0.0211	0.0053	0.007	0.0062
Sb4	0.3505(4)	0.0869(4)	0.8219(5)	0.011(5)	0.0134	0.0309	0.0248	0.0106	0.01	0.013

Table 4. Atomic distances and angles of kermesite.

Atom–Atom	Distances (Å)	Atom–Atom–Atom	Angles	Atom–Atom–Atom	Angles
Sb(1)-O(1)	2.160(3)	**O(1) [1]-Sb(2)-O(2)**	143.4(9)°	**S(3)-Sb(3)-S(2)**	94.3(3)°
Sb(1)-O(2)	2.030(2)	**O(1) [1]-Sb(2)-S(2)**	87.3(7)°	**S(3)-Sb(4)-S(4) [3]**	95.4(3)°
Sb(1)-O(2) [2]	2.150(2)	**O(1)-Sb(1)-S(1)**	85.6(7)°	**S(4)-Sb(4)-S(3)**	91.2(3)°
Sb(2)-O(1)	2.010(2)	**O(1)-Sb(2)-O(1) [1]**	71.9(11)°	**S(4)-Sb(4)-S(4) [3]**	86.6(3)°
Sb(2)-O(1) [1]	2.140(3)	**O(1)-Sb(2)-O(2)**	73.3(9)°	**Sb(1) [2]-O(2)-Sb(2)**	141.1(11)°
Sb(2)-O(2)	2.170(2)	**O(1)-Sb(2)-S(2)**	97.0(7)°	**Sb(1)-O(2)-Sb(1) [2]**	107.2(10)°
Sb(1)-S(1)	2.493(9)	**O(2) [2]-Sb(1)-O(1)**	141.4(9)°	**Sb(1)-O(2)-Sb(2)**	106.2(10)°
Sb(2)-S(2)	2.478(9)	**O(2) [2]-Sb(1)-S(1)**	84.0(6)°	**Sb(1)-S(1)-Sb(3) [1]**	106.4(3)°
Sb(3)-S(1) [1]	2.515(9)	**O(2)-Sb(1)-O(1)**	73.1(9)°	**Sb(2) [1]-O(1)-Sb(1)**	143.3(12)°
Sb(3)-S(2)	2.538(9)	**O(2)-Sb(1)-O(2) [2]**	72.8(10)°	**Sb(2)-O(1)-Sb(1)**	107.4(11)°
Sb(3)-S(3)	2.454(9)	**O(2)-Sb(1)-S(1)**	101.4(7)°	**Sb(2)-O(1)-Sb(2) [1]**	108.1(11)°
Sb(4)-S(3)	2.620(9)	**O(2)-Sb(2)-S(2)**	86.0(6)°	**Sb(2)-S(2)-Sb(3)**	102.9(3)°
Sb(4)-S(4)	2.435(9)	**S(1) [1]-Sb(3)-S(2)**	102.6(3)°	**Sb(3)-S(3)-Sb(4)**	101.1(3)°
Sb(4)-S(4) [3]	2.624(9)	**S(3)-Sb(3)-S(1) [1]**	94.3(3)°	**Sb(4)-S(4)-Sb(4) [3]**	93.4(3)°

Note: Symmetry codes [1] 1-x, y, z; [2] 1-x, 1-y, 1-z; [3] 2-x, 1-y, 2-z.

The collection of single-crystal structure data for kermesite spanned an angle 2θ range from 4.078° to 51.356°, encompassing a total of 1580 independent diffraction points. The single-crystal XRD diffractogram of kermesite, depicted in Figure 3, was generated using CrystalDiffract software version 6.9.4 by Crystalmaker Software Ltd. (Oxfordshire, UK). After refinement, the residual factors R1 and wR2 for the entire set of diffraction points were determined as 0.1000 and 0.2428, respectively. The refined results unveil the presence of twinning structures in kermesite from Yunnan, China, mirroring the findings in kermesite from Slovakia. As shown in Table 1, kermesite crystals from Yunnan exhibit a twinning content of 27.4%. In comparison, the twinning content in two Slovakian kermesite crystals, as reported by Hylber and Ďurovič (2013) [11], displays a notable discrepancy. One crystal exhibits a mere 5.46% twinning, while the other boasts a substantial 41.68%.

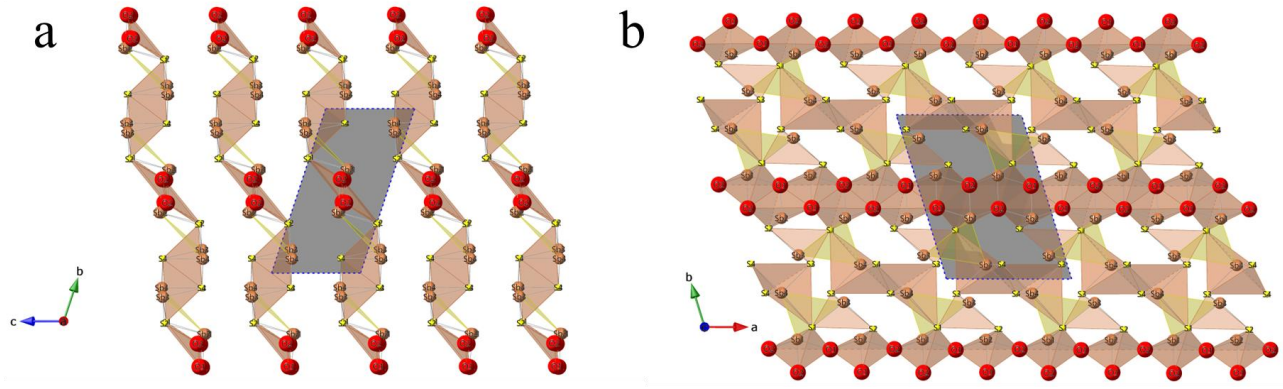

Figure 2. *Cont.*

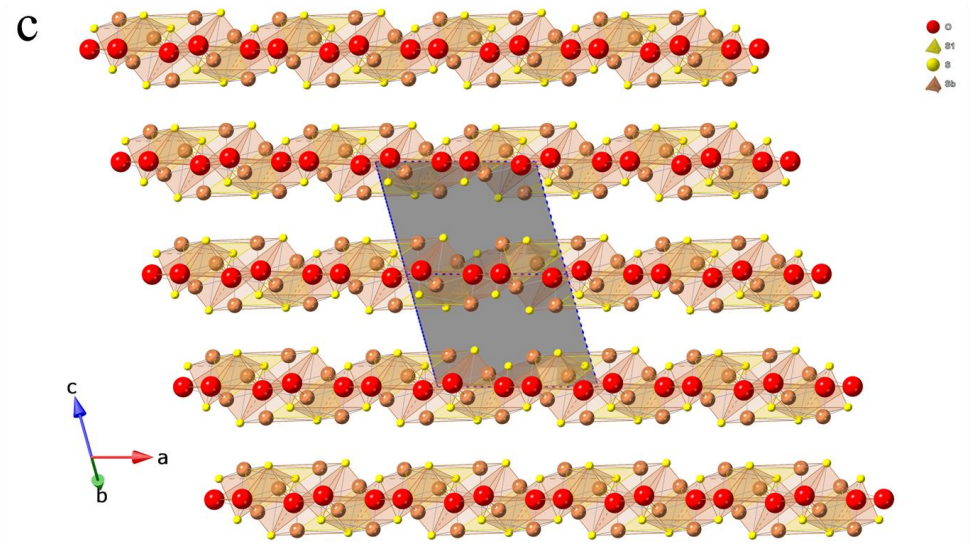

Figure 2. Structure of kermesite. (**a**,**b**) depict the structural projections along the a-axis and c-axis, respectively, while (**c**) shows the projection along the reciprocal axis b* in the ac plane. Drawing completed with CrystalMaker [17].

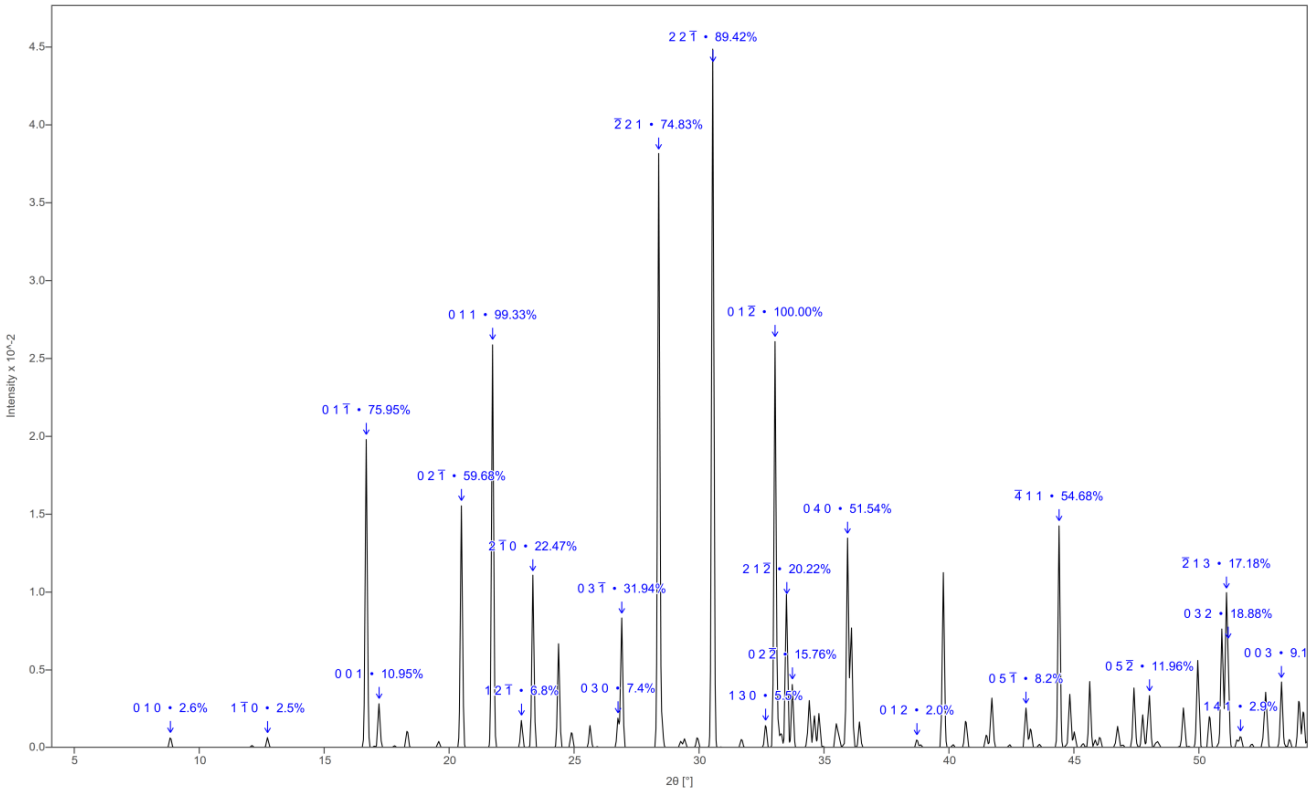

Figure 3. Single-crystal XRD diffractogram of kermesite. Generated using CrystalDiffract software [17].

3.3. Microstructure of Kermesite Crystals

Kermesite exhibits notable characteristics of parallel extinction, particularly along the {100} cleavage plane. Under cross-polarized light conditions in an optical microscope, well-defined plate-like striations become apparent, aligning parallel to the crystals' elongation direction. These striations, with lengths ranging in the hundreds of micrometers and extending up to several millimeters at their longest, are illustrated in Figure 4a,b. To further elucidate the relationship between the plate-like structures and the matrix, this study employed TEM for the direct observation and analysis of kermesite. Notably, there is a lack of prior literature reporting

kermesite using TEM. In this study, kermesite with plate-like features was prepared as TEM samples. After ion thinning, TEM revealed that the width of the plate-like structures within the kermesite matrix varied from 100 nm to 2000 nm, with the thinnest regions measuring only a few nanometers, as shown in Figure 4c–e. EDS demonstrated that the composition of the plate-like structures is identical to that of the matrix. Using SAED, an analysis was conducted on both the plate-like structures and the surrounding matrix. Figure 4d displays three sets of diffraction patterns (Figure 4(d1–d3)) with nearly indistinguishable orientations, showing slight intensity variations in individual diffraction spots.

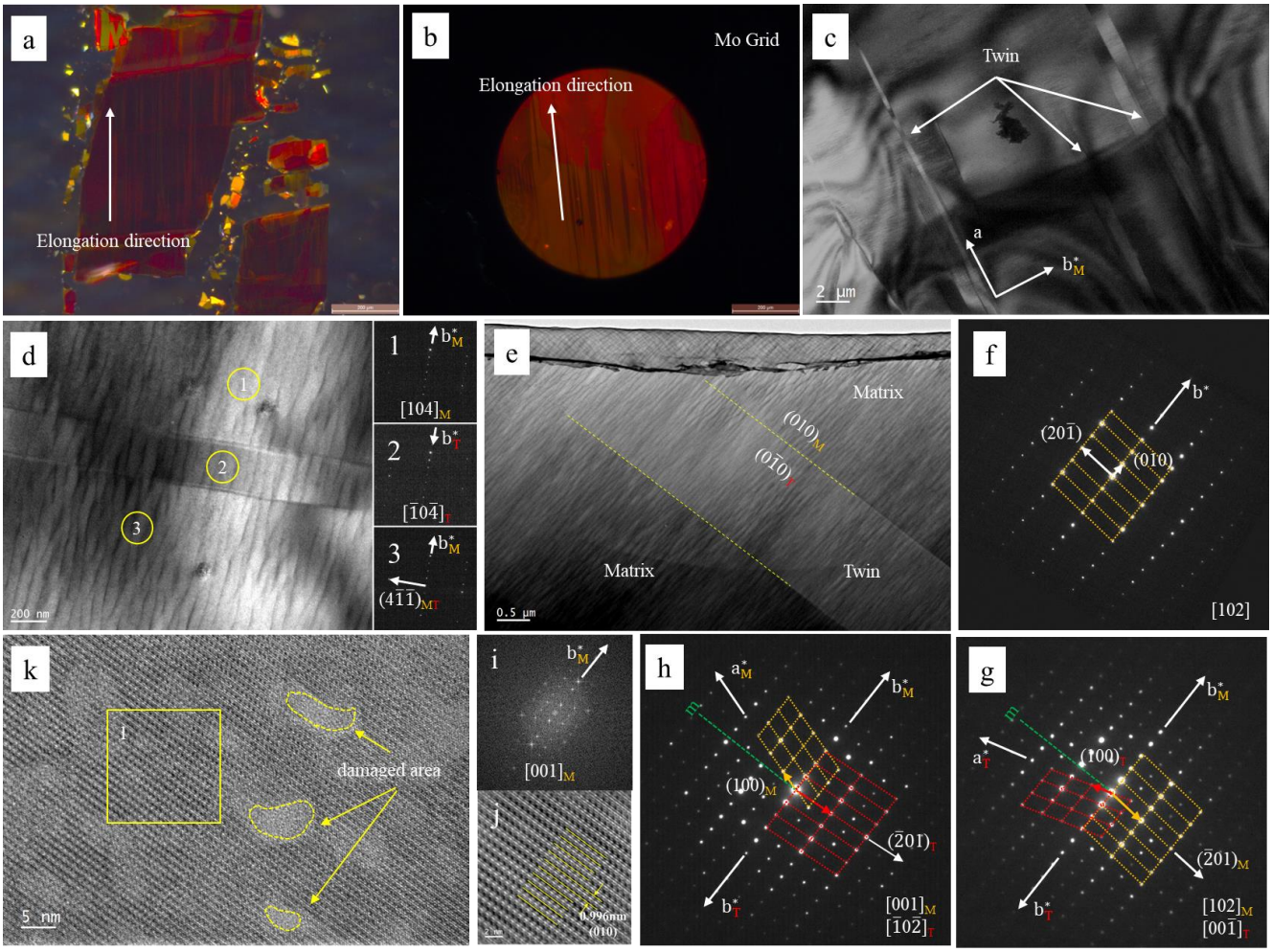

Figure 4. Microstructural images of kermesite. (**a**,**b**), under cross-polarized light in an optical microscope, kermesite exhibits a distinct laminar structure along its elongation direction. TEM analysis confirms the presence of twinning, with (**b**) representing a TEM sample with a molybdenum ring, yet to undergo ion thinning, and a scale bar of 200 μm. Images (**c**–**e**) present TEM photographs of twinning, with (**c**) indicating the respective SAED patterns at positions 1, 2, and 3. The three sets of SAED patterns show identical orientations with slight variations in diffraction spot intensities. Other SEAD patterns are shown in (**f**–**h**). (**f**,**g**) show diffraction patterns at the same zone axis for both the matrix and the twinning boundary. The orientation difference between (**h**) and (**g**) is 41.17°, indicating that the (001) plane of the kermesite matrix is parallel to the $(0\bar{1}\ 0)$ plane of the twin; further details of indexing can be found in Supplementary Figures S1 and S2. Image (**k**) presents a high-resolution view of kermesite along the [001] crystallographic direction. (**i**) shows the Fourier transform (FFT) of the boxed region in (**k**), and (**j**) displays the inverse Fourier transform (IFFT) of (**i**). The crystallographic directions a, b, and c and the reciprocal lattice vectors a* and b* are annotated for clarity. Additionally, the following abbreviations are used: M for matrix (color: orange); T for twin (color: red); m for mirror (color: green).

A systematic series of tilting experiments by TEM was conducted along specific Kikuchi lines to investigate identical locations on the boundary between the kermesite matrix and the plate-like structures. Multiple sets of SAED patterns were acquired during this tilt series. Examination of these SAED patterns revealed a noteworthy observation: in certain regions, the diffraction pattern of the matrix precisely coincided with both the diffraction pattern of the boundary and the three sets of diffraction patterns displayed in Figure 4d. Conversely, in other regions, some diffraction spots from the matrix partially overlapped with those of the plate-like structures. This indicated that the diffraction spots of one structural component only partially correlated with that of the other. Figure 4f,g illustrate the SAED patterns corresponding to the matrix and the boundary, respectively. The SAED pattern of the crystallographic interface is a composite of the patterns obtained from both the matrix and the plate-like structures. Upon superimposing a grid on the diffraction spots from both patterns, it becomes evident that the diffraction spots of the matrix (orange grid) constitute a portion of the diffraction spots of the plate-like structures (red grid), with the overlapping spots exhibiting significantly higher intensities than the non-overlapping ones.

In Figure 4g, under the crystal's zone axis, a tilt of 42.01° (TEM mechanical tilt angle) along a fixed Kikuchi line resulted in the diffraction pattern shown in Figure 4h on the crystallographic interface. Notably, the diffraction pattern of the plate-like structures (red grid) in this instance coincides with a portion of the diffraction pattern of the matrix (orange grid), contrasting with the pattern observed in Figure 4g. This observation compellingly supports the assertion that the plate-like structures observed in kermesite indicate twinning phenomena. It is noteworthy that the twinning plane determined by TEM in this study as $(\bar{4}11)$ aligns with the findings of Bonazzi et al. (1987), whose conclusions are based on refined X-ray single-crystal data from kermesite in Slovakia. Consequently, the presence of twinning imparts a pseudo-symmetry reminiscent of monoclinic crystal systems within the lattice.

Utilizing the refined single-crystal structure data presented in Table 1 (Column C) and aligning it with the diffraction patterns in Figure 4, where M and T represent the matrix and twinning, respectively, the investigation reveals that all three sets of diffraction patterns were acquired by tilting along the {010} Kikuchi line. This establishes a consistent orientation relationship of $(010)_M \| (0\bar{1}0)_T$. Upon closer examination of the diffraction spots, it becomes evident that the $[102]_M \| [00\bar{1}]_T$ in Figure 4g and $[001]_M \| [\bar{1}0\bar{2}]_T$ in Figure 4h exhibit mirror symmetry. This mirror plane is identified as parallel to {010}, denoted by the green-marked mirror plane m in the image. The a^*_M and a^*_T symmetrically flank this mirror, resulting in the mirror-symmetric arrangement of the diffraction spot $(2\bar{1}\bar{1})_M \| (200)_T$ in Figure 4g and the diffraction spot $(200)_M \| (2\bar{1}\bar{1})_T$ in Figure 4h.

We further investigated the stacking arrangement of kermesite's crystal structure. In the high-resolution TEM image along the [001] zone axis, it is evident that kermesite exhibits stacking along {010} layers. The interlayer spacing, directly measured from the Inverse Fast Fourier Transform (IFFT) image is determined to be 9.93 Å. Kermesite displays high sensitivity to electron beams, and under an operating voltage of 200 kV, even brief exposure results in sample damage, as illustrated by the irregular circles in Figure 4k. A few seconds of electron beam irradiation leads to localized amorphization of kermesite, posing challenges in utilizing high-resolution imaging for direct observation and analysis of the interrelationship between the matrix and twinning in kermesite.

4. Discussion

4.1. The Influence of Twinning on Structural Analysis

Twinning refers to the intersection of two adjacent crystals with a specific orientation relationship, giving rise to new macroscopic symmetry elements such as reflection planes, rotation axes, or symmetry centers [20–24]. Kermesite crystals belong to the low-symmetry monoclinic crystal system. Studies utilizing single-crystal XRD and TEM have revealed the presence of twinning in kermesite crystals from Yunnan, China. The existence of twinning introduces symmetry elements, such as mirror planes or rotated symmetry elements, which

are absent in the original crystal. This may lead to misinterpretations in structural analysis or the determination of primary unit cells. As highlighted by Bonazzi P et al. (1987), who first identified twinning in kermesite single crystals, the initial determination of the crystal structure by Wolfe C W in 1939 proposed symmetry elements involving secondary rotation axes and mirror planes [6,9]. Although Tavora (1949) and Kupčìκ (1967) later recognized that kermesite exhibits only monoclinic symmetry, their assigned unit cells were complex monoclinic structures [9,10]. This misinterpretation arose because of the lack of awareness regarding the presence of twinning in single crystals, impacting the accurate characterization of the crystal structure.

A comprehensive analysis of the twinning system in kermesite was conducted, as depicted in Figure 5. We combined the obtained series of SAED patterns, as shown in Figure 5a. For ease of observation and analysis, the composite series of SAED patterns were rotated counterclockwise by 37°, aligning the (010) Kikuchi line horizontally. Figure 5(a1,a6) correspond to Figures 4h and 4g, respectively, while Figure 5(a4) correspond to the three sets of diffraction patterns in Figure 4d. It is evident that Figure 5(a1,a6) are symmetrical to Figure 5(a4), with a mechanical tilt angle of 21.03° (calculated as 20.59°), consistent with the analysis of $[102]_M \| [00\bar{1}]_T$ in Figure 4g and $[001]_M \| [\bar{1}0\bar{2}]_T$ in Figure 4h based on diffraction spots. By reconstructing multiple unit cells of kermesite and twinning based on the orientation relations in Figure 5a ($(\bar{4}11)$ as the twinning plane, $(010)_M \| (0\bar{1}0)_T$, $[104]_M \| [\bar{1}0\bar{4}]_T$), as illustrated in Figure 5b,c, it is evident that the b-axis vectors of the matrix and twinning are parallel, $[100]_M \| [100]_T$. This suggests that twinning in kermesite from Yunnan, China, is a rotation twin, the twinning plane is $(\bar{4}11)$, and it is generated by a 180° rotation around the [100] axis, indicating the twinning axis.

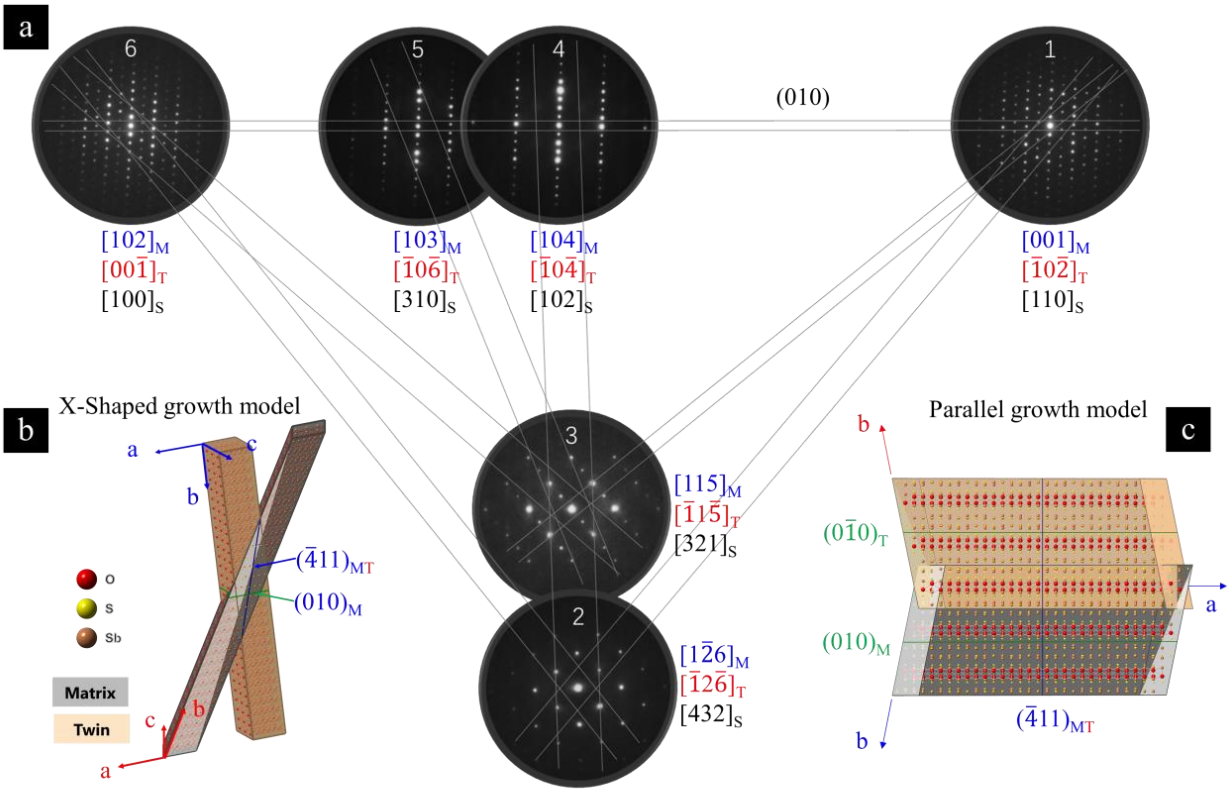

Figure 5. *Cont.*

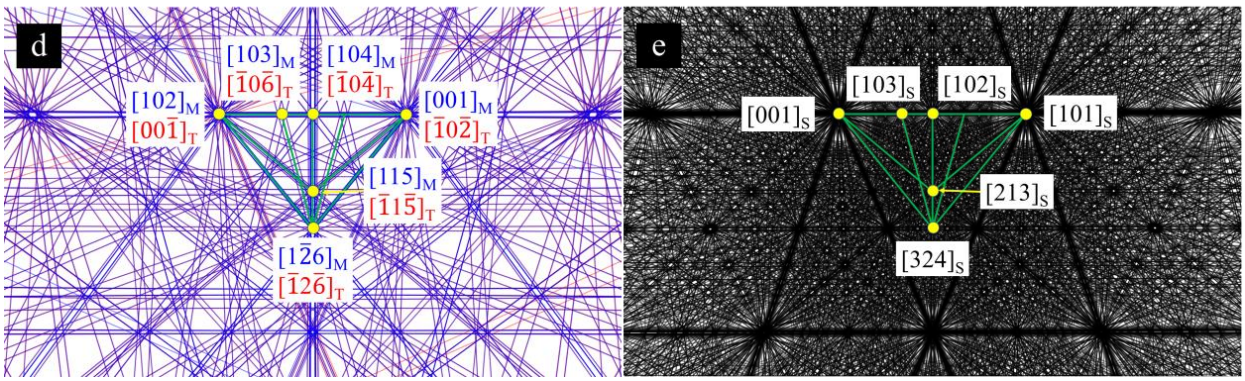

Figure 5. SAED patterns and structural simulation of kermesite. (**a**) Calibration and reconstruction of a series of SAED patterns, with blue indicating the indexing of the matrix, red indicating twinning, and black representing the structural indexing of the reconstructed TEM diffraction patterns. (**b**) Schematic representation of the structure of the kermesite matrix and twinning along the c-axis elongation axis, with a unit cell ratio of a:b:c = 3:50:3. The $(\bar{4}11)_{MT}$ plane denotes the twinning plane, and $(010)_M \| (0\bar{1}0)_T$. (**c**) Representation of the atomic stacking at the boundary between the kermesite matrix and twinning, based on the diffraction pattern 4 in (**a**), with a unit cell ratio of a:b:c = 7:3:3. The $(\bar{4}11)_{MT}$ plane overlaps between the matrix and twinning, while the (010) plane of the matrix is parallel to the $(0\bar{1}0)$ plane of the twinning, and the atomic arrangement is nearly identical. (**d**,**e**) represent indexed Kikuchi patterns based on the calibration in (**a**), where (**d**) shows the nearly complete overlap of the Kikuchi lines of the kermesite matrix (blue) and its twinning (red), and (**e**) displays the Kikuchi spectra of the reconstructed TEM electron diffraction patterns, fully overlapping with (**d**). M: matrix (color: blue); T: twin (color: red); S: structure rebuilding as a new phase (color: black). Generated using CrystalMaker [17] and SingleCrystal [25].

In an attempt to reconstruct and simulate the series of SAED patterns in Figure 5a as a new structure, we used the reported structure of kermesite as a tentative reference. We found that the structure submitted by Tavora E in 1949 aligns well with all SAED patterns [9]. The simulated unit cell parameters are a = 11.97 Å, b = 9.37 Å, c = 11.42 Å, α = 111.7°, β = 92.67°, and γ = 110.7°, with space group $P\bar{1}$ and Z = 8. The black crystallographic axes in Figure 5a are annotated to represent the simulated structure.

Although the simulated structure lacks the symmetry operations of a monoclinic crystal system, pseudo-monoclinic mirror symmetry is observed along the $(\bar{2}11)$ Kikuchi line. Kikuchi maps are advantageous for visually assessing the spatial orientation differences between different structures. Therefore, by comparing the Kikuchi patterns simulated based on the overlap of diffraction patterns for the matrix and twinning, as shown in Figure 4d,e, it is evident that the Kikuchi patterns of the matrix (blue) and twinning (red) can be almost perfectly overlapped, while the Kikuchi patterns of the simulated structure also perfectly match those of the matrix and twinning. This indicates that the failure to detect the existence of twinning may lead to the misindexing of kermesite using a simulated structure.

4.2. Twinning Constraints on the Crystal Growth of Kermesite

In previous reports, the orientation of kermesite crystal growth was uniformly delineated as occurring along the long axis, resulting in platy or needle-like morphologies [1,6]. However, the present study introduces a subtle perspective, particularly evident in specimens sourced from Yunnan, China. Contrary to the prevailing paradigm, the OM images in Figure 4a,b distinctly portray platy twinning structures aligned parallel to the {010} plane. Given that TEM observes the cleavage planes of kermesite, exhibiting a laminar cleavage structure, and the SAED patterns were acquired with the TEM optical axis approximately perpendicular to these cleavage planes, a logical deduction positions the short axis of the cleavage planes along the c-axis. Consequently, the extension direction of kermesite, representing the elongation of $[Sb_2S_2O_4]_n$ chains, aligns with the a-axis.

In the context of $(010)_M \| (0\bar{1}0)_T$ and $[104]_M \| [\bar{1}0\bar{4}]_T$, we reconstructed the growth mode of kermesite crystals using multiple primary unit cells, as illustrated in Figure 5c. The ratio of unit cell parameters is a:b:c = 7:3:3. The simulated growth of both the matrix and the twin along the $[Sb_2S_2O_4]_n$ chains (a-axis) reveals a coexisting parallel growth mode, resembling the growth patterns observed in Figure 1c. However, in the single-crystal aggregates of kermesite, part of the crystals exhibit an intersecting growth pattern, forming a distinctive X-shaped structure, as shown in Figure 1b. Utilizing multiple primary unit cells and reconstructing along the long axis growth direction, with a ratio of a:b:c = 3:50:3, results in a pronounced X-shaped structure, as shown in Figure 5b. This suggests that the kermesite crystal clusters are formed through the combined influence of kermesite crystals and twins. Maybe part of kermesite single crystals grow along the long-axis direction, and when crystals encounter each other or face obstacles during the growth process, $(\bar{4}11)[100]$-type twinning begins to develop. This leads to the elongation of the $[Sb_2S_2O_4]_n$ chains in twinned crystals, while some kermesite single crystals continue to grow along the long axis, eventually forming aesthetically pleasing crystal clusters.

5. Conclusions

In summary, our pioneering study on kermesite crystals, especially those from Yunnan, China, challenges conventional assumptions about their structure and growth. Significantly, this is the first-ever application of TEM to investigate natural kermesite crystals, revealing novel insights into its structural complexities and growth mechanisms. The elongation direction of kermesite aligns with the extension direction of the $[Sb_2S_2O_4]_n$ chains (a-axis), challenging the traditional belief that crystal elongation occurs along the long axis (b-axis). Importantly, the identification of rotational twinning, specifically the $(\bar{4}11)[100]$-type observed directly, provides new perspectives on the crystallographic orientations of kermesite.

Through detailed analysis, incorporating single-crystal XRD, TEM observations, and crystallographic reconstructions, we have uncovered a subtle coexistence of matrix and twinning structures. This study highlights the significant influence of twinning on kermesite growth, with TEM revealing varied twinned structure dimensions, ranging from 100 nm to several millimeters. Moreover, the reconstruction growth modes, especially the coexisting parallel growth observed in crystal clusters, as shown in Figures 1c and 5c, highlight the intricate relationship between single crystals growing along the long axis and twinned crystals growing along the extension direction of the $[Sb_2S_2O_4]_n$ chain. This interaction results in aesthetically pleasing crystal clusters with an X-shaped structure, as shown in Figures 1b and 5b.

Furthermore, the comparison of experimental data with simulated structures emphasizes the importance of considering twinning phenomena in crystallographic investigations. The potential misinterpretations that may arise without acknowledging the presence and impact of twinning underscore the significance of this study. It not only advances our understanding of the structural complexities and growth mechanisms of kermesite but also underscores the necessity of re-evaluating reported crystallographic orientations and growth mechanisms in similar mineralogical investigations. The findings contribute valuable knowledge to the broader field of mineralogy and crystallography.

Supplementary Materials: The following supporting information can be downloaded at: https://www.mdpi.com/article/10.3390/min14050505/s1, Figure S1: SAED indexing corresponding to Figure 4g or Figure 5(a1); Figure S2: SAED indexing corresponding to Figure 4h or Figure 5(a6).

Author Contributions: Conceptualization, H.Y. and D.W. (Denghong Wang); formal analysis, H.Y. and D.W. (Dong Wang); funding acquisition, D.W. (Denghong Wang), Y.L. and C.K.; investigation, H.Y., D.W. (Dong Wang) and Z.C.; methodology, H.Y., D.W. (Denghong Wang), Z.Z. and W.L.; resources, D.W. (Denghong Wang); supervision, W.L.; writing—original draft, H.Y.; writing—review and editing, D.W. (Denghong Wang), Z.Z., W.L., Y.L. and C.K. All authors have read and agreed to the published version of the manuscript.

Funding: This research was funded by the project "Geology of mineral resources in China" from China Geological Survey (Grant No. DD20221695, DD20190379, DD20160346), National Key R&D Program of China (project 2022YFC2905301), Chinese National Natural Science Foundation (grants 42072114), and Baotou Iron and Steel Company Project Funds (HE2224, HE2228, HE2312, HE2313).

Data Availability Statement: Data are contained within this article.

Acknowledgments: This manuscript benefitted from helpful discussions with Yong-lei Wang, Shun-da Yuan, Weibing Liao, Hong-zhang Dai, Jin-hua Qin, Lin-yue Sun, and anonymous reviewers of ACS Omega. We thank Xiao-dan Chen, Chun-hua Liu, Zhi-jian Niu, and Ze Liu for their help during the experiments. We also thank anonymous reviewers and academic editors for their constructive comments, which greatly improved this manuscript.

Conflicts of Interest: The authors declare no conflicts of interest.

References

1. Cairncross, B. Connoisseur's Choice: Kermesite, Globe and Phoenix Mine, Kwekwe District, Zimbabwe. *Rocks Miner.* **2020**, *95*, 440–446. [CrossRef]
2. Schoeller, W. Observations on the alteration products of stibnite. *J. Mineral. Soc.* **1941**, *26*, 94–96. [CrossRef]
3. Baumgardt, E.M.; Kupcik, V. Synthesis of kermesite Sb_2S_2O. *J. Cryst. Growth* **1977**, *37*, 346–348. [CrossRef]
4. Wang, Y.; Wang, D.; Wang, Y.; Xu, J.; Ding, J.; Cai, J.; Huang, F.; Dai, H.; Liang, T.; Wang, D.; et al. *Antimony Ore Volume*; Geological Press House: Beijing, China, 2022; p. 30.
5. Kaufmann, A.B.; Lazarov, M.; Weyer, S.; Stevko, M.; Kiefer, S.; Majzlan, J. Changes in antimony isotopic composition as a tracer of hydrothermal fluid evolution at the Sb deposits in Pezinok (Slovakia). *Min. Depos.* **2023**, *59*, 559–575. [CrossRef]
6. Hybler, J.; Durovic, S. Kermesite, Sb_2S_2O: Crystal structure revision and order-disorder interpretation. *Acta Crystallogr. B* **2013**, *69*, 570–583. [CrossRef] [PubMed]
7. Sejkora, J.O.; Vitálo, J.T.; Čejka, J.Ď. Schafarzikite from the type locality Pernek (Male Karpaty Mountains, Slovak Republic) revisited. *Eur. J. Miner.* **2007**, *19*, 419–427. [CrossRef]
8. Castroviejo, R. Kermesite (ker). In *A Practical Guide to Ore Microscopy—Volume 1: Mineral Identification*; Castroviejo, R., Ed.; Springer International Publishing: Cham, Switzerland, 2023; pp. 405–408.
9. Bonazzi, P.; Menchetti, S.; Sabelli, C. Structure refinement of kermesite: Symmetry, twinning, and comparison with stibnite. Neues Jahrb. *Mineral. Monatsh* **1987**, *12*, 557–567.
10. Kupčík, V. Die Kristallstruktur des Kermesits, Sb_2S_2O. *Naturwissenschaften* **1967**, *54*, 114. [CrossRef]
11. Ďurovič, S.; Hybler, J. OD structures in crystallography—Basic concepts and suggestions for practice. *Z. Krist.-Cryst. Mater.* **2006**, *221*, 63–76. [CrossRef]
12. Mindat. Available online: https://www.mindat.org/min-2187.html (accessed on 7 April 2024).
13. Sheldrick, G. SHELXT—Integrated space-group and crystal-structure determination. *Acta Crystallogr. A* **2015**, *71*, 3–8. [CrossRef]
14. Dolomanov, O.V.; Bourhis, L.J.; Gildea, R.J.; Howard, J.A.K.; Puschmann, H. OLEX2: A complete structure solution, refinement and analysis program. *J. Appl. Crystallogr.* **2009**, *42*, 339–341. [CrossRef]
15. Sheldrick, G. Crystal structure refinement with SHELXL. *Acta Crystallogr. C* **2015**, *71*, 3–8. [CrossRef]
16. Herbst-Irmer, R. Twinning. In *Crystal Structure Refinement: A Crystallographer's Guide to SHELXL*; Oxford University Press: Oxford, UK, 2006; pp. 106–149. [CrossRef]
17. Palmer, D.C. Visualization and analysis of crystal structures using CrystalMaker software. *Z. Für Krist.-Cryst. Mater.* **2015**, *230*, 559–572. [CrossRef]
18. Shannon, R. Revised effective ionic radii and systematic studies of interatomic distances in halides and chalcogenides. *Acta Crystallogr. Sect. A* **1976**, *32*, 751–767. [CrossRef]
19. Kharbish, S.; Libowitzky, E.; Beran, A. Raman spectra of isolated and interconnected pyramidal XS3 groups (X = Sb,Bi) in stibnite, bismuthinite, kermesite, stephanite and bournonite. *Eur. J. Miner.* **2009**, *21*, 325–333. [CrossRef]
20. Aquilano, D.; Bruno, M.; Rubbo, M.; Pastero, L.; Massaro, F.R. Twin Laws and Energy in Monoclinic Hydroxyapatite, Ca5(PO4)3(OH). *Cryst. Growth Des.* **2015**, *15*, 411–418. [CrossRef]
21. Rubbo, M.; Bruno, M.; Massaro, F.R.; Aquilano, D. The Five Twin Laws of Gypsum ($CaSO_4 \cdot 2H_2O$): A Theoretical Comparison of the Interfaces of the Penetration Twins. *Cryst. Growth Des.* **2012**, *12*, 3018–3024. [CrossRef]
22. Rubbo, M.; Bruno, M.; Aquilano, D. The (100) Contact Twin of Gypsum. *Cryst. Growth Des.* **2011**, *11*, 2351–2357. [CrossRef]
23. Lu, K. Stabilizing nanostructures in metals using grain and twin boundary architectures. *Nat. Rev. Mater.* **2016**, *1*, 16019. [CrossRef]
24. Parsons, S. Introduction to twinning. *Acta Crystallogr. Sect. D* **2003**, *59*, 1995–2003. [CrossRef]
25. Palmer, D. SingleCrystal 4: Real-time multi-phase diffraction simulation. *J. Appl. Crystallogr.* **2020**, *53*, 860. [CrossRef]